# Optimized Averaged Kaczmarz Framework for Efficient Multi-Orientation Inversion in Quantitative Susceptibility Mapping

Sejal Maisheri, Ambedkar Dukkipati, and Phaneendra K. Yalavarthy, *Senior Member, IEEE*

***Abstract*— *Objective:*** **Quantitative Susceptibility Mapping (QSM) faces challenges due to the ill-posed nature of the inverse problem, which necessitates multi-orientation (MO) acquisitions to resolve susceptibility ambiguities. However, existing MO methods have several practical limitations. 1) Calculation Of Susceptibility through Multiple Orientation Sampling (COSMOS) requires four to five orientations, resulting in prohibitively long scan times that are unsuitable for clinical use. 2) Nonlinear Dipole Inversion (NDI) requires substantial computational resources for gradient evaluations across all orientations at each iteration and lacks systematic validation. This study aims to facilitate the clinical adoption of MO-QSM methods. *Methods:* This study proposes the Optimized Multi-orientation Nonlinear Inversion of Susceptibility (OMNIS), a QSM reconstruction approach that integrates averaged Kaczmarz-style iterative updates with a nonlinear data fidelity formulation. Our proposed approach computes only a single-orientation gradient per iteration while preserving MO information. Furthermore, this study introduced an idealized MO simulated dataset with a known ground truth and provided comprehensive validation across simulated and *in vivo* datasets. *Results:* The proposed method achieves an approximately 80% reduction in total gradient evaluations and 50% reduction in runtime compared to the NDI, without requiring additional parameters or regularization. It maintains the same reconstruction quality while requiring fewer orientations, thereby reducing the scan time. Validation demonstrated statistically significant relative reductions in the NRMSE (11.5% mean) and HFEN (13.5% mean), along with reduced streaking artifacts and enhanced robustness in clinically relevant regions. *Conclusion:* OMNIS achieves improved reconstruction quality while reducing both computational burden and acquisition requirements, thereby providing a practical and clinically viable method for MO QSM reconstruction. *Significance:* The proposed method could enhance the diagnosis and monitoring of various diseases through reliable and feasible susceptibility estimation.**

***Index Terms*— Averaged Kaczmarz method, dipole inversion, image reconstruction, inverse problems, multiple orientations, quantitative susceptibility mapping (QSM)**

Part of this work is supported through Axis Bank Centre for Mathematics and Computing, Indian Institute of Science, Bangalore.

Sejal Maisheri is with IISc Mathematics Initiative, Indian Institute of Science, Bengaluru, 560012, Karnataka India (e-mail: sejalm@iisc.ac.in)

Ambedkar Dukkipati is with Department of Computer Science and Automation, Indian Institute of Science, Bengaluru, 560012, Karnataka India (e-mail: ambedkar@iisc.ac.in)

Phaneendra K. Yalavarthy is with Department of Computational and Data Science, Indian Institute of Science, Bengaluru, 560012, Karnataka India (e-mail: yalavarthy@iisc.ac.in)

## I. Introduction

QUANTITATIVE susceptibility mapping (QSM) is an advanced magnetic resonance imaging (MRI) technique that noninvasively quantifies the amount and spatial distribution of magnetic susceptibility using gradient-echo MRI [1]. Magnetic susceptibility refers to the degree of magnetization of a material in an external magnetic field. QSM can distinguish paramagnetic and diamagnetic substances through positive and negative susceptibility values, which are visualized as regions of high and low contrast, respectively, thereby enabling improved tissue characterization and reliable differentiation between hemorrhage and calcification. The quantitative nature of QSM provides clinically relevant biomarkers of tissue composition and pathological changes, including iron accumulation [2], myelin content [3], and venous oxygenation [4]. Consequently, QSM has important applications in the assessment of neurodegenerative disorders, evaluation of multiple sclerosis lesion activity, and estimation of the cerebral oxygen extraction fraction, providing valuable structural and functional information beyond that of conventional MRI techniques [5]. Given the increasing burden of these conditions, with Parkinson's disease estimated to affect over 25 million individuals worldwide by 2050 [6] and Alzheimer's disease expected to exceed 19 million cases by 2036 [7], QSM is of increasing clinical importance.

Multiple preprocessing steps are involved in obtaining the susceptibility map from the acquired MR phase data, including phase unwrapping, background field removal, and dipole inversion. Phase unwrapping resolves the ambiguity inherent in the measured phase's $2\pi$ periodicity, whereas background field removal eliminates unwanted phase contributions, such as those from air-tissue interfaces, to obtain the local field. Among these, dipole inversion is the most challenging step, in which the susceptibility map is obtained by deconvolving the unit dipole kernel from the local field via pointwise division in the Fourier domain. The presence of zeros in the dipole kernel on conical surfaces in the Fourier domain makes the reconstruction an ill-posed inverse problem, and direct inversion results in severe noise amplification and streaking artifacts in the image. Regularization techniques and priors, such as total variation, sparsity, smoothness, and gradient

constraints, stabilize the inversion by restricting feasible solution spaces. However, balancing data fidelity and regularization is inherently challenging, and the simplified assumptions encoded by such explicit regularizers may not fully reflect the true susceptibility distribution, potentially introducing a reconstruction bias [8], [9].

A more fundamental approach is to improve the conditioning of the inverse problem using complementary measurements. One such established method is the Calculation Of Susceptibility through Multiple Orientation Sampling (COSMOS), which acquires MR data from several object orientations relative to the main magnetic field [10] and estimates susceptibility using a closed-form solution. However, COSMOS typically requires four to five feasible *in vivo* orientations to effectively suppress streaking artifacts [11], resulting in an approximately 400% increase in total scan time. This substantially increases the patient burden due to prolonged scanning and repeated repositioning, also raising the risk of incomplete examinations, making such multi-orientation methods impractical for clinical use. Moreover, COSMOS relies on a linear field-to-susceptibility formulation that assumes Gaussian noise behavior, whereas the statistics of the MR phase noise differ considerably in low-SNR regions [12].

To address the limitations of linear inversion, nonlinear data fidelity formulations were introduced in [12]. Building on this framework, Nonlinear Dipole Inversion (NDI) [13] applies a nonlinear relation to multi-orientation (MO) settings and reports improved reconstruction quality over COSMOS under limited orientations, with comparable performance at higher sampling. However, these conclusions were primarily based on visual assessments and lacked quantitative validation owing to the absence of a ground truth. In addition, the NDI relies on a computationally intensive gradient-descent optimization scheme that requires gradient evaluations for all orientations at each iteration, leading to multiple Fourier-domain transformations and high computational cost.

To overcome these limitations, we integrated the Averaged Kaczmarz (AVEK) [14] optimization method within a multi-orientation QSM reconstruction framework with a nonlinear data-fidelity formulation, resulting in OMNIS (Optimized Multi-orientation Nonlinear Inversion of Susceptibility). AVEK decomposes the MO objective into sequential orientation-specific updates, retaining information from all orientations through iterative averaging of intermediate updates, and each iteration requires only a single-orientation gradient evaluation, thereby making it computationally efficient for MO methods. To systematically validate the MO QSM methods, we extended an available realistic simulation framework [15] to an MO setting by generating data from eight distinct head orientations. Using the known simulated ground truth, we performed direct quantitative comparisons of the COSMOS, NDI, and proposed OMNIS methods.

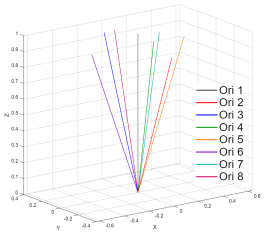
The main contributions of this study are as follows.

- We propose a novel optimization framework for multi-orientation QSM reconstruction for effective utilization of MO information and computational efficiency.
- We develop an idealized MO simulated QSM dataset and, to the best of our knowledge, present the first systematic validation of MO QSM methods.
- We perform a comprehensive evaluation using quantitative analysis, visual assessment, region-of-interest (ROI) analysis, and *in vivo* experiments to assess reconstruction performance and practical applicability.
- We establish the clinical applicability of the proposed framework and its potential to serve as an *in vivo* reference map by demonstrating the requirement of fewer orientations, reliable estimation in clinically relevant regions, improved agreement with ground truth, better preservation of fine structural details, reduced streaking artifacts, and improved computational efficiency compared to iterative methods.

The notations used in this study are summarized in Table I.

TABLE I
IMPORTANT NOTATIONS

| Symbol | Description |
|---|---|
| | **Theory Notations** |
| $\chi$ | Susceptibility map ($\chi*$ : Optimal susceptibility map) |
| $y$ | Local field map |
| $D$ | Dipole kernel (forward operator) |
| $N$ | Number of orientations |
| $W$ | Noise weighting map derived from signal magnitude |
| $\mathbf{b}_p$ | Main magnetic field vector in the object frame for orientation $p$ |
| | **Iterative Algorithm Notations** |
| $\alpha$ | Step size |
| $\tau$ | Gradient tolerance |
| $\delta$ | Relative gradient difference |
| $I_{\max}$ | Maximum number of iterations |




| | Field Coordinates ( $b_p$) | Rotation Detail |
|---|---|---|
| **Ori 1** | [0,0,1] | 0° |
| **Ori 2** | [0, -0.3746, 0.9272] | 22° about X-axis |
| **Ori 3** | [0, 0.3746, 0.9272] | -22° about X-axis |
| **Ori 4** | [0, -0.1736, 0.9848] | 10° about X-axis |
| **Ori 5** | [-0.3746, 0, 0.9272] | 22° about Y-axis |
| **Ori 6** | [0.3746, 0, 0.9272] | -22° about Y-axis |
| **Ori 7** | [0.1736, 0, 0.9848] | 10° about Y-axis |
| **Ori 8** | [0, 0.2588, 0.9659] | -15° about X-axis |

(A) (B)

Fig. 1. Description of the eight orientations (Ori) used for the MO simulation. (a) $\mathbf{b_p}$ visualization (b) Corresponding parameters.

## II. BACKGROUND

### A. QSM Forward Model

Quantitative Susceptibility Mapping (QSM) uses MRI phase measurements to estimate the underlying tissue susceptibility distribution $\chi(\mathbf{r})$. Under the influence of an external magnetic field $\mathbf{B}_0$, biological tissue with susceptibility $\chi(\mathbf{r})$ becomes magnetized and generates local magnetic field perturbations $\Delta b(\mathbf{r})$. This local field perturbation is obtained from the MRI signal phase after preprocessing and is related to the susceptibility distribution via convolution with the unit dipole kernel $D(\mathbf{r})$:

$$\Delta b(\mathbf{r}) = D(\mathbf{r}) * \chi(\mathbf{r}) \tag{1}$$

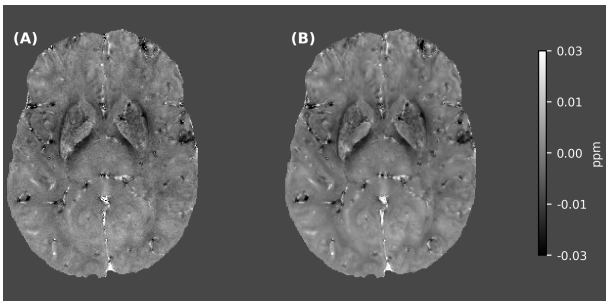



Fig. 2. Simulated local field maps for the SIM1 susceptibility model at orientation 1 under two noise settings: (a) SNR1 (peak SNR = 100) and (b) SNR2 (peak SNR = 1000). ppm stands for parts per million.

where $*$ denotes convolution and $\mathbf{r}$ denotes spatial coordinates. In the Fourier domain, Eq. (1) becomes a point-wise multiplication, allowing susceptibility estimation as

$$\chi(\mathbf{k}) = \frac{\Delta b(\mathbf{k})}{D(\mathbf{k})} \tag{2}$$

where $\mathbf{k} = (k_x, k_y, k_z)$ denotes the spatial frequency coordinates. For the usual case where the main magnetic field is oriented along the $z$-axis, i.e., $\mathbf{B}_0 = [0, 0, 1]^T$, the dipole kernel is

$$D(\mathbf{k}) = \frac{1}{3} - \frac{k_z^2}{\|\mathbf{k}\|^2} \tag{3}$$

Direct inversion of Eq. (2) is unstable because $D(\mathbf{k})$ vanishes on the conical surface defined by $k_x^2 + k_y^2 - 2k_z^2 = 0$. Values of $D(\mathbf{k})$ near zero cause severe noise amplification and streaking artifacts, rendering susceptibility estimation an ill-posed inverse problem [8], [9].

For simplicity, we denote $\chi(\mathbf{r})$ by $\chi$, $\Delta b(\mathbf{r})$ by $y$, and define the forward operator as $D = \mathcal{F}^{-1} D(\mathbf{k}) \mathcal{F}$ where $\mathcal{F}$ and $\mathcal{F}^{-1}$ denote the discrete forward and inverse Fourier transforms, respectively. The optimal Susceptibility $(\chi^*)$ reconstruction is commonly formulated as

$$\chi^* = \arg\min_{\chi} \|D\chi - y\|_2^2 \tag{4}$$

### B. Calculation Of Susceptibility through Multiple Orientation Sampling (COSMOS)

The ill-conditioning of single-orientation QSM can be alleviated by acquiring measurements at multiple object orientations relative to the direction of $\mathbf{B}_0$.

In the object reference frame, the forward model for orientation $p$ is

$$\Delta b_p(\mathbf{k}) = D_p(\mathbf{k})\chi(\mathbf{k}) \tag{5}$$

where the orientation-dependent dipole kernel is

$$D_p(\mathbf{k}) = \frac{1}{3} - \frac{(\mathbf{k} \cdot \mathbf{b}_p)^2}{\|\mathbf{k}\|^2} \tag{6}$$

Combining measurements from $N$ orientations, COSMOS [10] solves

$$\chi^* = \arg\min_{\chi} \sum_{p=1}^{N} \|D_p\chi - y_p\|_2^2 \tag{7}$$

which admits the closed-form solution

$$\chi_{cosmos} = \left(\sum_{p=1}^{N} D_p^T D_p\right)^{-1} \left(\sum_{p=1}^{N} D_p^T y_p\right) \tag{8}$$

As the number of orientations increased, the null regions of the rotated dipole kernels no longer overlapped, which substantially improved conditioning. This closed-form solution produces high-quality susceptibility reconstruction without the need for regularization. However, four to five feasible *in vivo* head orientations are typically required to substantially reduce the streaking artifacts [11].

The formulation in Eq. (4) assumes Gaussian noise in the field measurements. However, phase noise exhibits complex behavior: it is approximately Gaussian at a high SNR and becomes more uniform in low-signal regions, whereas intermediate regimes lack such simple approximations [12].

### C. Nonlinear Relationship Formulation and Nonlinear Dipole Inversion (NDI)

To better model the phase noise characteristics, nonlinear formulations [12] reconstruct the susceptibility by minimizing the discrepancies in the complex exponential domain as follows:

$$\chi^* = \arg\min_{\chi} \|W(e^{iD\chi} - e^{iy})\|_2^2 \tag{9}$$

Extending this formulation to multi-orientation reconstruction, NDI [13] defines

$$f(\chi) = \sum_{p=1}^{N} \|W_p(e^{iD_p\chi} - e^{iy_p})\|_2^2 \tag{10}$$

and solves it using a gradient descent iterative approach

$$\chi_{t+1} = \chi_t - 2\alpha \sum_{p=1}^{N} D_p^T W_p^T W_p \sin(D_p\chi_t - y_p) \tag{11}$$

The number of iterations acts as an implicit regularization, whereas the weighting map and nonlinear relation serve as inherent priors. The use of $W$ has been shown to mitigate noise amplification and streaking artifacts [16]. NDI was the first nonlinear MO reconstruction framework to challenge the COSMOS-level reconstruction quality. However, the evaluation was primarily qualitative and focused on visually reducing streaking artifacts.

## III. Methods and Materials

### A. Proposed Method: Optimized Multi-orientation Nonlinear Inversion of Susceptibility (OMNIS)

OMNIS is based on the AVEK-style [14] iterative regularization framework. Unlike full-gradient methods such as NDI, which require the evaluation of all orientation-dependent gradients at each iteration, OMNIS performs updates using only a single orientation while recursively incorporating information from the most recent $N$ orientation-specific auxiliary iterations.

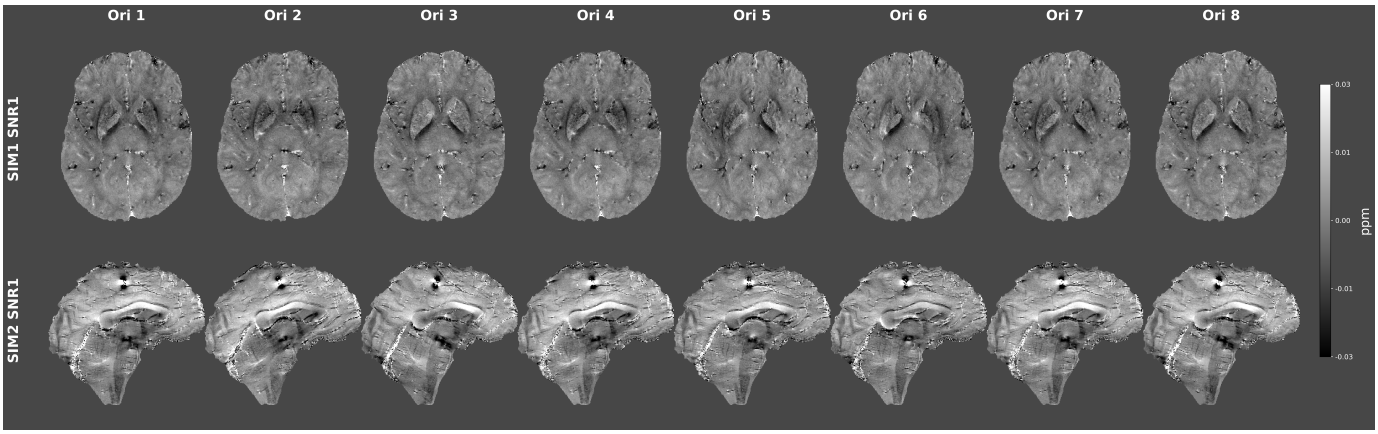



Fig. 3. Simulated local field maps for both susceptibility models at SNR1 across the eight orientations, see Fig. 1 for orientation details.

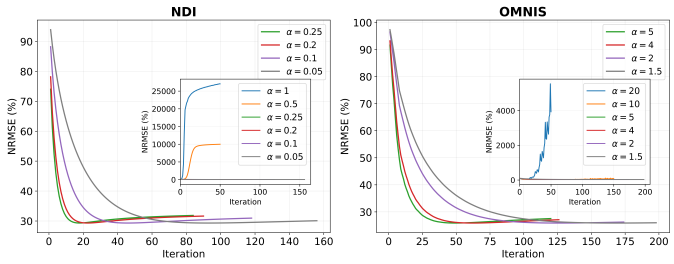



Fig. 4. Step-size sensitivity analysis of NDI and OMNIS on the SIM1 SNR1 dataset with $N = 8$. The tested $\alpha$ values are indicated in the legends. Insets show divergence for some $\alpha$ values, while the main plots show NRMSE trajectories until convergence.

For iteration $k$, let $[k] = ((k-1) \bmod N) + 1$ denote the active orientation. The iterative updates are then given by

$$\xi_k = \chi_{k-1} - 2\alpha D_{[k]}^T W_{[k]}^T W_{[k]} \sin(D_{[k]}\chi_{k-1} - y_{[k]}) \quad (12)$$

$$\chi_k = \chi_{k-1} + \frac{1}{N}(\xi_k - \xi_{k-N}) \quad (13)$$

Because OMNIS evaluates only a single orientation-specific gradient per iteration, its computational complexity is reduced by a factor of $N$ compared with NDI, while requiring only modest additional memory to store auxiliary variables. The complete iterative procedure is summarized in Algorithm 1. The convergence properties of the AVEK framework were established in a previous study [14]. Equal weighting of the auxiliary iterates was used and found to be optimal; assigning higher weights to the first orientations did not lead to significant improvements in the results.

**Algorithm 1** OMNIS

**Input:** $\{y_p, D_p, W_p\}_{p=1}^N$, $\alpha$, $\tau$, $I_{\max}$
**Initialize:** susceptibility map $\chi_0 = 0$, auxiliary variables $\xi_p = 0$, gradients $G_p = 0$, counter $c = 0$
**for** $k = 1, \ldots, I_{\max}$ **do**
  $[k] \leftarrow ((k-1) \bmod N) + 1$ // Active Orientation
  $G \leftarrow 2D_{[k]}^T W_{[k]}^T W_{[k]} \sin(D_{[k]}\chi_{k-1} - y_{[k]})$
  $\xi \leftarrow \chi_{k-1} - \alpha G$
  $\chi_k \leftarrow \chi_{k-1} + \frac{1}{N}(\xi - \xi_{[k]})$
  $\delta \leftarrow \frac{100\|G - G_{[k]}\|_2}{\|G\|_2}$ // Gradient difference (%)
  $\xi_{[k]} \leftarrow \xi$
  $G_{[k]} \leftarrow G$
  **if** $\delta < \tau$ **then** $c \leftarrow c+1$ **else** $c \leftarrow 0$ // Stopping Criterion
  **if** $c = 2N$ **then break**
**end for**
**Output:** $\chi_k$
**Stopping criterion:** Counter $c$ is incremented only when the relative gradient difference satisfies $\delta < \tau$. If the condition is violated for any orientation, $c$ is reset to zero to ensure that the stopping criterion is satisfied for all the orientations. The algorithm terminates when the criterion is satisfied for all $N$ orientations over two consecutive passes ($c = 2N$) or until the maximum iteration limit $I_{\max}$ is reached.

## B. Multi-Orientation Simulation Dataset

Quantitative assessment provides an objective evaluation of reconstruction fidelity, enabling the direct measurement of accuracy, error magnitude, and structural preservation relative to the known ground truth. Without ground truth, visual assessment alone is subjective and insufficient for rigorous evaluation. Thus, we generated a simulated multi-orientation dataset with known susceptibility ground truth by extending the RC2 simulation framework [15], which was released as part of the *2019 QSM Reconstruction Challenge* [17]. Specifically, we adapted the framework to simulate data for eight distinct head orientations. The orientation set consisted of independent rotations about the $X$- or $Y$-axis within the practically *in vivo* feasible head rotation range of $\pm 22°$, following [11]. The corresponding main field directions $\mathbf{b}_p$ in the object reference frame are shown in Fig. 1.

The RC2 framework provides two realistic *in silico* head susceptibility phantoms, SIM1 and SIM2. Both susceptibility models were synthesized from data acquired from a human volunteer, with SIM2 containing an intra-hemispheric calcification and exhibiting a stronger gray-white matter susceptibility contrast than SIM1. We followed the RC2 Challenge protocol for signal simulation and QSM preprocessing, except that the simulations were performed using the original high-

resolution data rather than the downsampled version provided in the challenge release.

We simulated spoiled gradient-recalled-echo MRI signals using the steady-state signal equation parameterized by *in vivo* $R_1$, $R_2^*$, and proton density $M_0$ maps. We added Gaussian noise to the simulated signals at two levels corresponding to peak SNRs of 100 (SNR1) and 1000 (SNR2), resulting in four datasets: SIM1 SNR1, SIM1 SNR2, SIM2 SNR1, and SIM2 SNR2. The peak SNR variable as per the RC2 framework is defined relative to the maximum signal intensity of the first echo. Each dataset comprised multi-echo magnitude and phase data simulated using the following acquisition parameters: field strength = 7T, repetition time (TR) = 50 ms, echo times ($TE_1/TE_2/TE_3/TE_4$) = 4/12/20/28 ms, flip angle $\alpha = 15°$, field of view (FOV) = $164 \times 205 \times 205$ mm$^3$, matrix size = $256 \times 320 \times 320$, and isotropic voxel size = 0.64 mm.

We implemented preprocessing using the SEPIA (1.2.2.6 version) toolbox [18]. We performed phase unwrapping using SEGUE [19], followed by a multi-echo phase combination using the optimal weighted averaging strategy described in [20] to obtain the final local-field map. Because the signal simulation was restricted to the brain-extracted region, background field removal (BFR) was not performed, which is consistent with the RC2 Challenge protocol. We additionally generated weighting maps using the standard SEPIA weighting formulation, which was not included in the original challenge.

A visual comparison of the local field maps obtained for SNR1 and SNR2 is presented in Fig. 2, whereas those corresponding to the eight head orientations at SNR1 are depicted in Fig. 3.

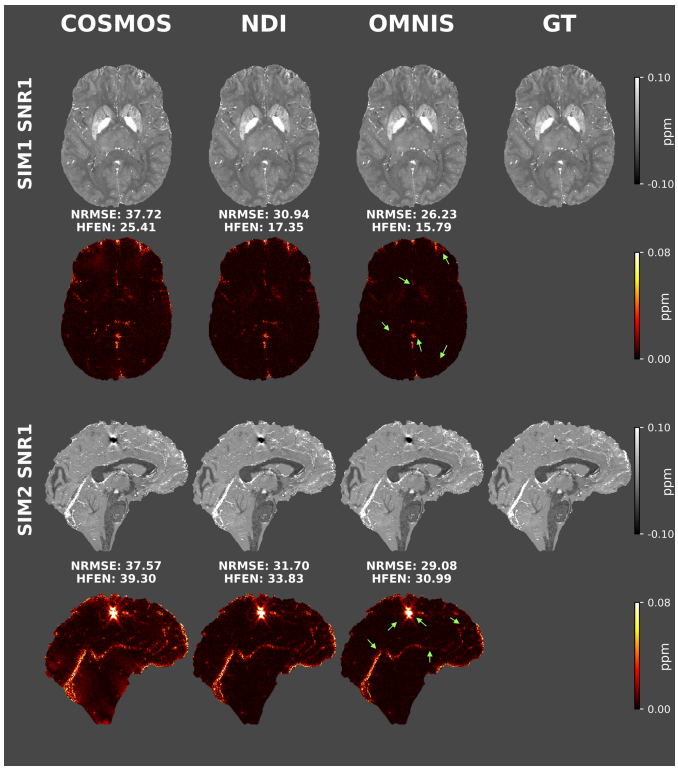



Fig. 5. QSM reconstruction using all eight orientations (N = 8) for COSMOS, NDI, and the proposed OMNIS framework, together with the ground truth (GT) and corresponding absolute error maps. The green arrows indicate regions with reduced error intensity and diminished streaking artifacts. NRMSE (%) and HFEN (%) relative to GT are shown below each reconstruction (see Table II for complete quantitative results).

### C. In Vivo Dataset

We performed *in vivo* evaluation to assess the ability of the proposed framework to generate anatomically meaningful susceptibility maps under realistic acquisition conditions. The dataset was obtained from the *2016 QSM Reconstruction Challenge* [21] and acquired from a healthy volunteer using a 3T Siemens TIM Trio system (Siemens Healthcare GmbH, Erlangen, Germany) with a 3D gradient-recalled echo (GRE) sequence and wave-CAIPI [22] acceleration. The acquisition parameters included an isotropic voxel size of 1.06 mm, TR of 35 ms, TE of 25 ms, and bandwidth of 100 Hz/pixel. The dataset consisted of local field maps acquired across 12 distinct head orientations, along with a magnitude image, brain mask, region-wise segmentation mask and COSMOS map.

### D. Implementation Details

We generated multi-orientation simulated datasets using MATLAB R2025b and performed validation experiments using MATLAB R2026a software. We evaluated the reconstruction performance using different numbers of orientations, where $N = k$ denotes reconstruction using the first k orientations, hereafter referred to as orientation settings.

Publicly available implementations of COSMOS and NDI were used for the comparison. For the NDI, the reported step size of $\alpha = 1$ did not converge on the simulated datasets, as the relative gradient difference ($\delta$) initially decreased slightly, followed by an increase and subsequent plateau. Therefore, we tuned the step size for the NDI. The step sizes for OMNIS and NDI were empirically determined based on the convergence behavior and computational efficiency using the SIM1 SNR1 dataset with $N = 8$, and were fixed at $\alpha = 2$ and $\alpha = 0.1$, respectively, for all simulated datasets and orientation settings. Figure 4 shows the sensitivity of NRMSE to the choice of $\alpha$, with NRMSE trajectories plotted as a function of the number of iterations until convergence for each tested convergent $\alpha$ for both methods.

For the *in vivo* dataset, the step sizes determined from the simulated experiments resulted in lower susceptibility contrast. Consequently, the original step size of $\alpha = 1$ was used for NDI, whereas $\alpha = 10$ was selected for OMNIS based on the visual contrast and the monotonic decrease in $\delta$. Following the NDI, the gradient tolerance was fixed at $\tau = 1\%$. The maximum number of iterations was set sufficiently high such that convergence was achieved according to the gradient tolerance criterion for all datasets.

## IV. Results

### A. Quantitative and Visual Evaluation

We assessed the reconstruction fidelity using the normalized root mean square error (NRMSE), peak signal-to-noise ratio

TABLE II

QUANTITATIVE PERFORMANCE UNDER SNR1 FOR SIMULATED DATASETS. N=K DENOTES RECONSTRUCTION USING THE FIRST K ORIENTATIONS. THE BEST RESULTS ARE IN **BOLD**. QUALITATIVE COMPARISONS CORRESPONDING TO THESE RESULTS ARE SHOWN IN FIGS. 5 AND 6.

| N | Method | SIM1 SNR1 | | | | SIM2 SNR1 | | | |
|---|---|---|---|---|---|---|---|---|---|
| | | NRMSE (%) ↓ | PSNR (dB) ↑ | SSIM ↑ | HFEN (%) ↓ | NRMSE (%) ↓ | PSNR (dB) ↑ | SSIM ↑ | HFEN (%) ↓ |
| 8 | COSMOS [10] | 37.7240 | 38.7617 | 0.97690 | 25.4096 | 37.5659 | 55.4613 | 0.99801 | 39.2999 |
| | NDI [13] | 30.9447 | 40.4824 | **0.98327** | 17.3466 | 31.6983 | 56.9364 | 0.99853 | 33.8346 |
| | OMNIS (prop.) | **26.2308** | **41.9179** | 0.98097 | **15.7857** | **29.0833** | **57.6843** | **0.99887** | **30.9898** |
| 7 | COSMOS | 39.4047 | 38.3831 | 0.97445 | 26.0516 | 38.2199 | 55.3114 | 0.99782 | 39.5379 |
| | NDI | 32.6541 | 40.0153 | **0.97924** | 18.1159 | 32.4090 | 56.7438 | 0.99838 | 34.1371 |
| | OMNIS | **27.6850** | **41.4492** | 0.97897 | **16.3642** | **29.6712** | **57.5104** | **0.99875** | **31.2881** |
| 6 | COSMOS | 40.8766 | 38.0646 | 0.97199 | 26.5906 | 38.8072 | 55.1789 | 0.99763 | 39.5167 |
| | NDI | 34.2029 | 39.6128 | **0.97911** | 18.8871 | 33.0605 | 56.5710 | 0.99823 | 34.2098 |
| | OMNIS | **29.0873** | **41.0200** | 0.97745 | **16.8923** | **30.2368** | **57.3464** | **0.99862** | **31.3746** |
| 5 | COSMOS | 45.6157 | 37.1118 | 0.97489 | 28.6858 | 41.4777 | 54.6009 | 0.99689 | 41.6872 |
| | NDI | 37.8991 | 38.7215 | **0.97956** | 20.9074 | 35.3830 | 55.9813 | 0.99776 | 36.1561 |
| | OMNIS | **32.6043** | **40.0286** | 0.97911 | **18.4359** | **32.2198** | **56.7947** | **0.99825** | **32.7413** |
| 4 | COSMOS | 61.8500 | 34.4673 | 0.95026 | 36.4051 | 50.7452 | 52.8493 | 0.99392 | 48.1307 |
| | NDI | 44.4991 | 37.3271 | **0.97257** | 27.1742 | 41.2258 | 54.6538 | 0.99694 | 41.3494 |
| | OMNIS | **39.8889** | **38.277** | 0.96865 | **24.1769** | **37.9083** | **55.3825** | **0.99745** | **37.3265** |
| 3 | COSMOS | 67.6335 | 33.6909 | 0.93951 | 38.9241 | 52.8967 | 52.4886 | 0.99296 | 47.6059 |
| | NDI | 47.7678 | 36.7114 | **0.96570** | 29.3827 | 42.4476 | 54.4001 | 0.99648 | 41.1799 |
| | OMNIS | **43.5508** | **37.5142** | 0.96296 | **25.7208** | **39.0308** | **55.1290** | **0.99705** | **36.9023** |
| 2 | COSMOS | 117.4515 | 28.8969 | 0.85171 | 60.9307 | 79.8811 | 48.9083 | 0.97829 | 62.7015 |
| | NDI | **54.8360** | **35.5128** | 0.95392 | 38.9264 | 49.0955 | 53.1363 | 0.99531 | 48.8338 |
| | OMNIS | 54.8750 | 35.5066 | **0.95467** | **32.3203** | **46.6221** | **53.5853** | **0.99546** | **42.6344** |

TABLE III

QUANTITATIVE PERFORMANCE UNDER SNR2 FOR SIMULATED DATASETS. N=K DENOTES RECONSTRUCTION USING THE FIRST K ORIENTATIONS. THE BEST RESULTS ARE IN **BOLD**.

| N | Method | SIM1 SNR2 | | | | SIM2 SNR2 | | | |
|---|---|---|---|---|---|---|---|---|---|
| | | NRMSE (%) ↓ | PSNR (dB) ↑ | SSIM ↑ | HFEN (%) ↓ | NRMSE (%) ↓ | PSNR (dB) ↑ | SSIM ↑ | HFEN (%) ↓ |
| 8 | COSMOS [10] | 21.1284 | 43.7968 | 0.99705 | 17.3577 | 32.2202 | 56.7946 | 0.99960 | 37.0281 |
| | NDI [13] | 9.0172 | 51.1926 | 0.99902 | 4.5795 | 25.8825 | 58.6970 | 0.99976 | 31.7530 |
| | OMNIS (prop.) | **7.7782** | **52.4765** | **0.99917** | **4.2668** | **24.4157** | **59.2038** | **0.99981** | **28.9802** |
| 7 | COSMOS | 21.3688 | 43.6985 | 0.99658 | 17.3948 | 32.3002 | 56.7731 | 0.99959 | 37.1321 |
| | NDI | 9.6181 | 50.6323 | 0.99885 | 4.8357 | 26.0076 | 58.6551 | 0.99975 | 31.8947 |
| | OMNIS | **8.2516** | **51.9634** | **0.99906** | **4.3539** | **24.5063** | **59.1716** | **0.99980** | **29.1099** |
| 6 | COSMOS | 21.4918 | 43.6486 | 0.99664 | 17.2431 | 32.3562 | 56.7580 | 0.99959 | 37.1557 |
| | NDI | 10.1652 | 50.1518 | 0.99883 | 5.0382 | 26.1081 | 58.6217 | 0.99975 | 31.9483 |
| | OMNIS | **8.7227** | **51.4810** | **0.99904** | **4.4512** | **24.5623** | **59.1518** | **0.99980** | **29.1208** |
| 5 | COSMOS | 22.4886 | 43.2548 | 0.99667 | 17.7967 | 33.296 | 56.5093 | 0.99951 | 38.6617 |
| | NDI | 11.6617 | 48.9589 | 0.99863 | 5.9672 | 27.0366 | 58.3181 | 0.99970 | 33.3090 |
| | OMNIS | **9.8331** | **50.4403** | **0.99892** | **4.9612** | **25.2395** | **58.9156** | **0.99977** | **30.1361** |
| 4 | COSMOS | 27.3147 | 41.5662 | 0.99307 | 20.9619 | 37.5416 | 55.4669 | 0.99898 | 43.4751 |
| | NDI | 20.2852 | 44.1505 | 0.99500 | 15.0847 | 32.8075 | 56.6377 | 0.99927 | 38.1999 |
| | OMNIS | **16.3215** | **46.0389** | **0.99709** | **10.6509** | **29.8524** | **57.4576** | **0.99949** | **34.0352** |
| 3 | COSMOS | 27.9411 | 41.3692 | 0.99334 | 20.8214 | 37.0301 | 55.5861 | 0.99901 | 41.8867 |
| | NDI | 21.6963 | 43.5664 | 0.99420 | 16.4147 | 32.8864 | 56.6168 | 0.99921 | 37.4441 |
| | OMNIS | **17.1728** | **45.5973** | **0.99687** | **11.0170** | **29.3982** | **57.5907** | **0.9995** | **32.8321** |
| 2 | COSMOS | 40.7792 | 38.0853 | 0.97179 | 29.3190 | 45.7618 | 53.7471 | 0.99650 | 50.7294 |
| | NDI | 31.3193 | 40.3778 | 0.98669 | 27.3296 | 39.3969 | 55.0479 | 0.99846 | 44.3118 |
| | OMNIS | **21.3195** | **43.7185** | **0.99678** | **14.0230** | **32.4270** | **56.7390** | **0.99933** | **37.0055** |

(PSNR), structural similarity index measure (SSIM), and high-frequency error norm (HFEN). Tables II and III summarize the reconstruction performance under the SNR1 and SNR2 noise settings, respectively. Across nearly all experimental settings, OMNIS outperformed COSMOS and NDI, achieving notable mean relative reductions of 11.5% in NRMSE and 13.5% in HFEN relative to NDI. For the SIM1 SNR1 case, OMNIS yielded marginally lower SSIM values for certain orientation settings; however, it maintained a competitive overall performance, with consistently achieving superior fine-structural

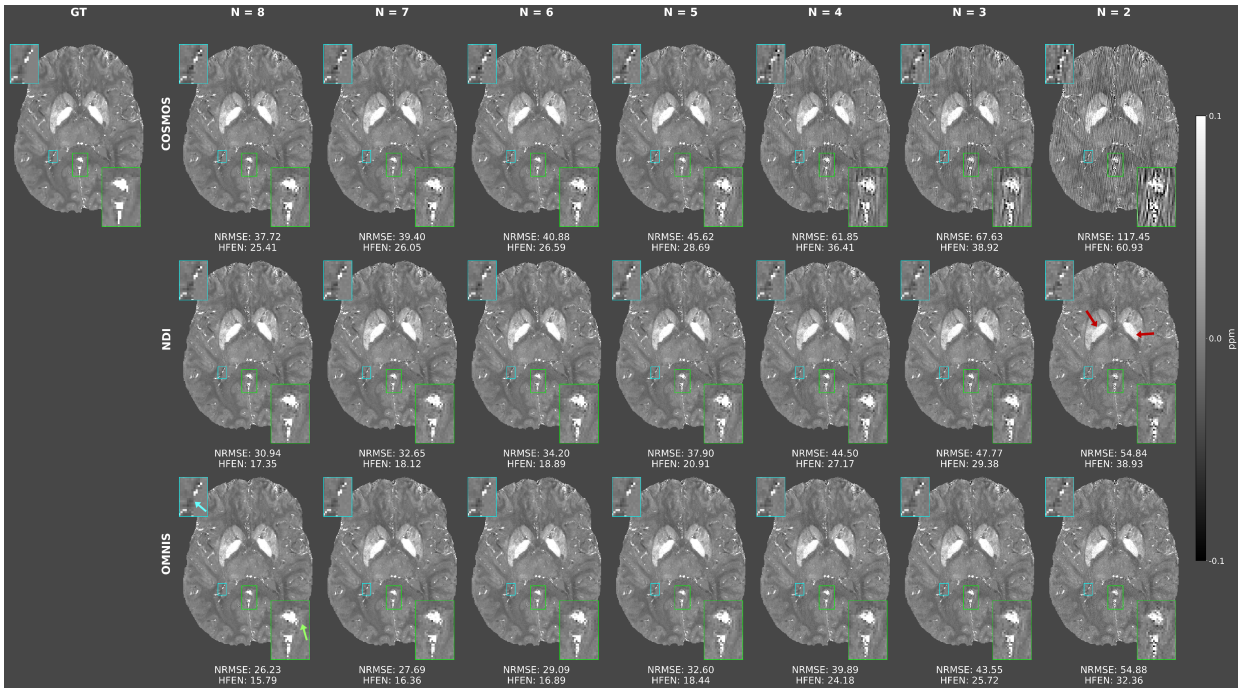



Fig. 6. QSM reconstruction for all orientation settings for SIM1 SNR1 dataset. The highlighted cyan and lime boxes are presented in enlarged views, with cyan and lime arrows indicating a closer agreement with the GT and diminished streaking artifacts, respectively. The red arrows highlight some inaccuracies in the NDI for N=2. NRMSE (%) and HFEN (%) relative to GT are shown below each reconstruction (see Table II for complete quantitative results).

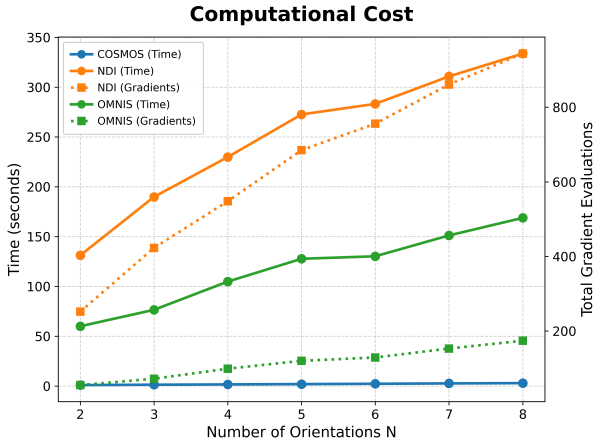



Fig. 7. Computational cost comparison across all orientation settings ($N$). The reported values are for the SIM1 SNR1 dataset, with NDI and OMNIS measured until convergence. The left $y$-axis shows reconstruction time (seconds), while the right $y$-axis shows the total number of gradient evaluations.

preservation and improved reconstruction accuracy. Paired two-sided Wilcoxon signed-rank tests were performed between OMNIS and NDI for both phantoms across all configurations (2 noise levels $\times$ 7 orientation settings , (n = 14)). The resulting $p$-values for SIM1 were $2.44 \times 10^{-4}$ for NRMSE, $1.22 \times 10^{-4}$ for HFEN, $2.44 \times 10^{-4}$ for PSNR, and 1 for SSIM, whereas those for SIM2 were $1.22 \times 10^{-4}$ for NRMSE, $1.22 \times 10^{-4}$ for HFEN, $1.22 \times 10^{-4}$ for PSNR, and $9.7 \times 10^{-4}$ for SSIM.

The visual comparisons shown in Figs. 5 and 6 further support these quantitative findings. Although these metrics provide global measures of image quality, the error maps in Fig. 5 enables a localized assessment of the reconstruction errors, where OMNIS exhibits reduced error levels and diminished streaking artifacts. Figure 6 further presents the reconstruction results across all orientation settings, with enlarged views of selected regions demonstrating closer agreement with the ground truth.

Figure 7 compares the computational cost across all orientation settings. Compared with the iterative method NDI, OMNIS required approximately five times fewer gradient evaluations, corresponding to an approximately 80% reduction, and reduced the reconstruction time by approximately 50%, demonstrating improved computational efficiency.

Since the RC2 challenge protocol uses a brain-extracted phantom for simulation and therefore does not involve BFR, we performed an additional experiment to further examine the robustness of OMNIS to residual fields resulting from BFR. We performed BFR using the Laplacian boundary value [23] method and obtained the residual field by subtracting the first orientation local field of the brain-extracted phantom from that of the whole-head phantom. The residual field was then added to the local fields of the other orientations. Table IV presents the quantitative results, where OMNIS achieved the best performance across all evaluated metrics, thus demonstrating its robustness to BFR errors.

## B. Region of Interest Analysis

We performed a region-of-interest (ROI) analysis of tissue regions that are less susceptible to orientation-dependent effects and are clinically relevant. Table V summarizes the ROI

reconstruction errors, where OMNIS achieved lower errors, indicating improved susceptibility estimation. Figure 8 shows scatter plots comparing reconstructed and reference susceptibility values in deep gray matter (DGM) subregions. OMNIS achieved a higher correlation and lower fitting error with fewer outliers and reduced scatter than the baseline methods.

### C. In Vivo Evaluation

Figure 9 compares *in vivo* reconstructions. The step sizes determined from the simulated experiments yielded lower susceptibility contrast for NDI and OMNIS, particularly for NDI at lower $N$, resulting in susceptibility underestimation and poorly distinguishable anatomical structures. Increasing the step size improved the contrast for both methods on the *in vivo* dataset. At lower orientation settings, COSMOS exhibited streaking artifacts, whereas NDI and OMNIS produced visually similar reconstructions with comparable consistency, and OMNIS required more than 50% less reconstruction time than NDI across all evaluated orientation settings. Table VI summarizes the mean and standard deviation of the susceptibility values measured in different regions using *in vivo* measurements at $N = 12$. All methods produced comparable susceptibility estimates, with NDI and OMNIS showing slightly smaller magnitudes than COSMOS, and OMNIS exhibiting lower relative variability in certain regions.

Considering the equivalence as $\alpha_{\mathrm{OMNIS}} = N * \alpha_{\mathrm{NDI}}$, the step sizes empirically tuned using the SIM1 SNR1 dataset at $N = 8$ show that the optimal OMNIS step size of $\alpha = 2$ corresponds to an effective $2/8 = 0.25$, which is a factor of 2.5 relative to the optimal NDI step size of $\alpha = 0.1$. However, for the *in vivo* data at $N = 12$, $\alpha_{\mathrm{OMNIS}} = 10$ corresponds to a factor of $10/12 = 0.83$ relative to the original NDI step size of $\alpha_{\mathrm{NDI}} = 1$. One approach for determining the step size for *in vivo* data in the absence of ground truth is to select a representative anatomical region and increase $\alpha$ among the convergent values until the regional mean susceptibility reaches a plateau. Table VII shows the sensitivity of the regional susceptibility values to $\alpha$ for OMNIS at $N = 12$, with saturation reached at approximately $\alpha = 40$. At $N = 12$, increasing $\alpha$ from 10 to 60 reduced the deficit relative to COSMOS from 2.9-8.9% to less than $1.5\%$ in five of the six DGM regions. However, as $\alpha = 40$ and $\alpha = 20$ did not converge at lower orientation settings, we retained $\alpha = 10$ for *in vivo* dataset for simplicity and consistency across all evaluated $N$. A similar saturation analysis could be applied to NDI; however, for consistency with the original evaluation, we retained the originally reported NDI step size for the *in vivo* dataset.

## V. Discussion

Multi-orientation QSM methods aim to improve susceptibility estimation through angular oversampling; however, the increased acquisition time associated with several head orientations limits their clinical application. Moreover, the absence of a known ground truth restricts quantitative evaluation, and the assessment of existing methods has largely been limited to visual inspection. In this study, we extended a realistic single-orientation QSM simulation framework [15] to MO settings, enabling a controlled quantitative assessment in the presence of a known ground truth.

Across quantitative metrics and visual assessments, OMNIS demonstrated overall superior performance relative to the baseline COSMOS [10] and NDI [13]. An important finding was the ability of OMNIS to achieve comparable or superior reconstruction quality with fewer orientations. Specifically, OMNIS with six orientations achieved lower NRMSE and HFEN values than COSMOS and NDI with eight orientations across all simulated datasets. Apart from mitigating streaking artifacts at lower orientation settings, OMNIS requires approximately three to five fewer orientations to achieve a quantitative performance comparable to COSMOS. Compared with NDI, OMNIS primarily modifies the iterative update strategy, reducing the number of gradient evaluations by approximately 80%, the reconstruction time by approximately 50%, and yielding improved reconstruction quality. The discrepancy between the reductions in gradient evaluations and reconstruction time may be attributed to parallelization of gradient evaluations across orientations in NDI, as well as auxiliary-iterate memory traffic and sequential orientation processing in OMNIS. An additional observation from the step-size sensitivity analysis performed on the SIM1 SNR1 dataset with $N = 8$ ( Fig. 4 ) is that, across the tested step sizes, the lowest achievable NRMSE was approximately 30% for NDI, compared with approximately 26% for OMNIS. Visual assessment further showed that OMNIS better preserved fine structural details while maintaining smooth susceptibility reconstructions without excessive over-smoothing.

A plausible explanation for the observed improvements is that because the NDI jointly aggregates information across all orientations at each iteration, orientation-specific measurement noise and anisotropy effects may propagate through the optimization process and adversely affect the preservation of fine details, as illustrated in Fig 6. In contrast, the proposed OMNIS formulation computes orientation-specific auxiliary iterates, which may better suppress the effects of measurement error, potentially by limiting the influence of individual perturbations on the averaged update, thereby enhancing structural consistency and preserving structural fidelity, which is consistent with the quantitative results in Tables II and III.

One limitation of the simulation framework is that only a single-orientation *in vivo* $R_2^*$ map was available and used for the signal generation across all orientations. Since $R_2^*$ exhibits orientation dependence in anisotropic tissue structures [24]–[26], particularly in the white matter, this may have introduced inaccuracies in the susceptibility estimation in anisotropic regions. Therefore, the ROI analysis was focused on regions where the limitation would have minimal impact, and OMNIS demonstrated a reduced reconstruction error and improved agreement with the reference susceptibility values in these regions. The reduced scatter and fewer outliers observed in the DGM regions in the scatter plots are clinically relevant, given that abnormal iron accumulation in the DGM is associated with several neurodegenerative disorders [5]. For instance, susceptibility alterations in the substantia nigra (SN) and subtha-

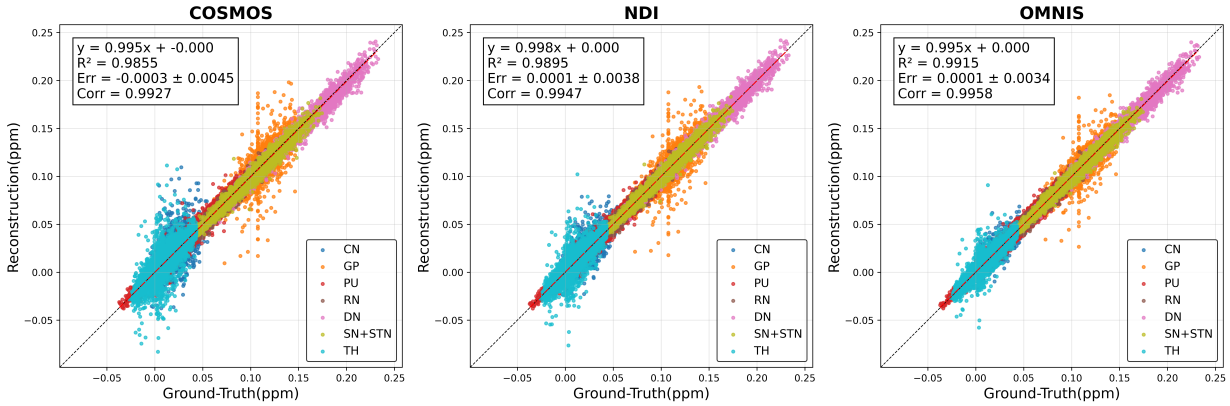



Fig. 8. Scatter plots of susceptibility values in deep gray matter regions with respect to the ground truth for SIM1 SNR1 dataset (N = 8). Seven regions of interest (ROIs) were identified: CN (caudate nucleus), GP (globus pallidus), PU (putamen), RN (red nucleus), DN (dentate nucleus), SN+STN (substantia nigra + subthalamic nucleus), and TH (thalamus); where y, $\boldsymbol{R^2}$, Err, and Corr denote the equation of the fitted regression line (red line), coefficient of determination, error, and Pearson's correlation, respectively. The black dotted line represents the ideal case.

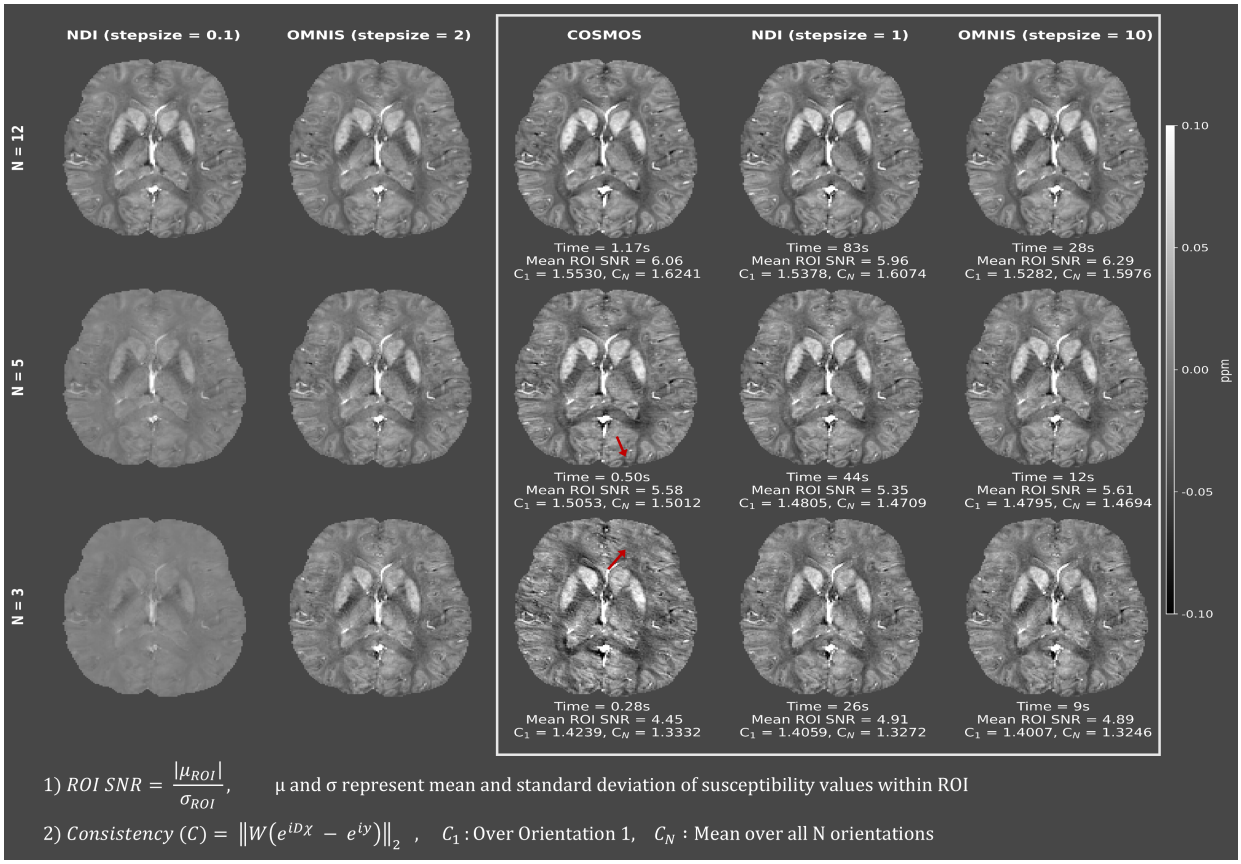



Fig. 9. QSM reconstructions on the *in vivo* dataset [21] using simulation-selected and increased step sizes. The red arrows highlight the streaking artifacts in COSMOS. Reconstruction time in seconds (s), Mean ROI SNR across the regions listed in Table VI, and consistency as defined in [13] are reported; metric definitions are provided at the bottom of the figure.

lamic nucleus (STN) have been reported as important imaging biomarkers for Parkinson's disease [27], [28]. Averaged across all four simulated datasets, OMNIS achieved a 6.56% relative reduction in susceptibility scatter and a 6.6% relative reduction in reconstruction error in the SN+STN region compared with NDI, indicating more reliable susceptibility estimation in these clinically important structures and thus increasing diagnostic confidence.

The *in vivo* experiments further demonstrated the feasibility of OMNIS under practical acquisition conditions. The differences in the optimal step size between the simulated and *in vivo* datasets may be attributed to variations in the acquisition parameters and the increased complexity of the real signal characteristics that are not fully represented in the simulation framework. However, as shown in Fig. 9, OMNIS appeared less sensitive to step size selection than NDI, maintaining a meaningful susceptibility contrast even with the step size

TABLE IV

QUANTITATIVE PERFORMANCE FOR SIM1 SNR1 SIMULATED USING WHOLE HEAD PHANTOM. THE BEST RESULTS ARE IN **BOLD**. RECONSTRUCTION TIME IS REPORTED IN SECONDS (S). GRADIENTS REPRESENT THE TOTAL GRADIENT EVALUATION TILL CONVERGENCE.

| N | Method | NRMSE (%) ↓ | PSNR (dB) ↑ | SSIM ↑ | HFEN (%) ↓ | Time (s) ↓ | Gradients ↓ |
|---|---|---|---|---|---|---|---|
| 8 | COSMOS [10] | 86.8758 | 32.1830 | 0.97884 | 59.3343 | 2.9 | - |
| | NDI [13] | 78.4222 | 33.0722 | 0.98455 | 54.0764 | 387 | 992 |
| | OMNIS (prop.) | **70.4188** | **34.0072** | **0.98575** | **49.3013** | 160 | 174 |
| 5 | COSMOS | 89.5894 | 31.9158 | 0.97639 | 59.8283 | 1.8 | - |
| | NDI | 79.6190 | 32.9406 | 0.98169 | 53.8320 | 301 | 750 |
| | OMNIS | **71.7592** | **33.8434** | **0.98367** | **48.9536** | 109 | 120 |
| 3 | COSMOS | 111.5941 | 30.0081 | 0.96672 | 70.9816 | 1.2 | - |
| | NDI | 82.1040 | 32.6673 | 0.98149 | 56.0446 | 200 | 453 |
| | OMNIS | **76.1101** | **33.3321** | **0.98244** | **51.4919** | 61 | 66 |

TABLE V

ROI-BASED ERROR (%). ∼WM DENOTES REGIONS EXCLUDING WHITE MATTER (WM), COMPRISING DEEP GRAY MATTER (DGM), GRAY MATTER (GM), CEREBROSPINAL FLUID (CSF), AND BLOOD VESSELS (BVS). THE BEST RESULTS ARE IN **BOLD**.

| N | Method | SIM1 SNR1 | | SIM2 SNR1 | | SIM1 SNR2 | | SIM2 SNR2 | |
|---|---|---|---|---|---|---|---|---|---|
| | | GM ↓ | ∼WM ↓ | GM ↓ | ∼WM ↓ | GM ↓ | ∼WM ↓ | GM ↓ | ∼WM ↓ |
| 8 | COSMOS | 0.4015 | 0.0575 | 0.5169 | 0.0731 | 0.2449 | 0.0327 | 0.3913 | 0.0523 |
| | NDI | 0.2857 | 0.0419 | 0.3023 | 0.0450 | 0.0536 | 0.0079 | 0.0722 | 0.0112 |
| | OMNIS (proposed) | **0.2559** | **0.0371** | **0.2708** | **0.0400** | **0.0452** | **0.0068** | **0.0648** | **0.0102** |
| 5 | COSMOS | 0.4822 | 0.0692 | 0.5929 | 0.0843 | 0.2548 | 0.0343 | 0.4058 | 0.0546 |
| | NDI | 0.3660 | 0.0532 | 0.3930 | 0.0577 | 0.0849 | 0.0122 | 0.1147 | 0.0168 |
| | OMNIS (proposed) | **0.3291** | **0.0472** | **0.3496** | **0.0509** | **0.0559** | **0.0084** | **0.0809** | **0.0125** |

TABLE VI

REGION-WISE SUSCEPTIBILITY VALUES (MEAN ± STANDARD DEVIATION) IN PARTS PER BILLION (PPB) FOR IN VIVO DATASET [21].

| Region | COSMOS | NDI | OMNIS |
|---|---|---|---|
| Caudate Nucleus | $62.36 \pm 11.39$ | $59.03 \pm 11.15$ | $56.81 \pm 10.20$ |
| Putamen | $84.19 \pm 15.49$ | $81.62 \pm 14.89$ | $80.00 \pm 13.39$ |
| Globus Pallidus | $188.70 \pm 25.96$ | $187.58 \pm 27.95$ | $180.62 \pm 23.64$ |
| Red Nucleus | $90.27 \pm 16.18$ | $89.48 \pm 17.56$ | $87.66 \pm 15.60$ |
| Substantia Nigra | $173.49 \pm 23.94$ | $171.03 \pm 22.80$ | $163.99 \pm 22.18$ |
| Dentate Nucleus | $117.67 \pm 12.71$ | $116.81 \pm 12.08$ | $112.91 \pm 11.22$ |
| White Matter | $-27.97 \pm 13.04$ | $-27.47 \pm 14.11$ | $-26.26 \pm 14.09$ |

TABLE VII

SENSITIVITY OF REGION-WISE SUSCEPTIBILITY VALUES (MEAN ± STANDARD DEVIATION) IN PARTS PER BILLION (PPB) FOR OMNIS WITH $N = 12$ ON THE IN VIVO DATASET [21].

| Label | $\alpha = 60$ | $\alpha = 40$ | $\alpha = 20$ | $\alpha = 10$ |
|---|---|---|---|---|
| CN | $58.98 \pm 11.23$ | $58.98 \pm 10.99$ | $58.86 \pm 10.90$ | $56.81 \pm 10.20$ |
| PU | $81.93 \pm 14.85$ | $81.66 \pm 14.74$ | $81.51 \pm 14.61$ | $80.00 \pm 13.39$ |
| GP | $187.60 \pm 28.18$ | $187.05 \pm 27.26$ | $186.56 \pm 26.83$ | $180.62 \pm 23.64$ |
| RN | $89.67 \pm 17.74$ | $89.23 \pm 17.37$ | $89.10 \pm 17.21$ | $87.66 \pm 15.60$ |
| SN | $171.12 \pm 22.87$ | $170.46 \pm 22.78$ | $169.96 \pm 22.76$ | $163.99 \pm 22.18$ |
| DN | $116.64 \pm 12.18$ | $116.62 \pm 11.97$ | $116.33 \pm 11.90$ | $112.91 \pm 11.22$ |

determined from the simulated dataset.

The simulation and *in vivo* experiments suggest the potential clinical applicability of OMNIS in QSM reconstruction. Improved susceptibility estimation in clinically important regions enhances the utility of OMNIS for disease characterization and assessment, facilitating its integration into clinical practice. By demonstrating a reduced orientation requirement, OMNIS can improve the practical feasibility of multi-orientation QSM by reducing the scan time, repeated patient repositioning, and the overall burden on the patient. Fast accelerated acquisition strategies, such as Wave-CAIPI [22], which substantially reduce the per-orientation scan time, can further improve the clinical feasibility of OMNIS. Additionally, denoising techniques for high-resolution complex GRE data [29] could improve the field map quality, enabling more accurate susceptibility estimation and better characterization of fine anatomical structures.

The ideal clinical scenario is an accurate QSM reconstruction using a single orientation. However, in the single-orientation setting, the averaging formulation used in OMNIS becomes less meaningful because no complementary orientation information is available for combination. Consequently, a substantial body of QSM research continues to focus on improving the single-orientation susceptibility estimation. Among these approaches are conventional methods, such as nMEDI [12], STAR-QSM [30], and HEIDI [31], which effectively mitigate noise and artifacts but require careful parameter tuning and carry an inherent risk of inaccurate estimation due to the missing information. Supervised deep learning methods, including QSMnet [32], MODL-QSM [33] and LPCNN [34], aim to learn a mapping from single-orientation measurements to MO reconstructions through paired training but often exhibit limited generalization. Deep learning (DL) has also been leveraged by autoQSM [35] and iQSM [36] to directly reconstruct QSM from unwrapped total field maps and raw phase data, respectively, to address error propagation between successive preprocessing steps. To improve the generalization of DL-based QSM reconstruction across acquisition condi-

tions, approaches have been proposed to address variations in acquisition orientation (iQSM+ [37]), spatial resolution (AdaIN-QSM [38]), or both (AFTER-QSM [39]). More recently, generative approaches, such as Diffusion-QSM [40], QSMDiff [41], and Flow-QSM [42], have learned the distribution of susceptibility maps from MO reference reconstructions, such as COSMOS, and subsequently performed subject-specific reconstruction by sampling from the learned distribution. Another line of research includes self-supervised methods, such as msQSM [43], and unsupervised methods, including INR-QSM [44] and MoDIP [45], which have demonstrated promising performance without requiring ground-truth data. However, challenges remain regarding the interpretability of the learned priors and computational efficiency, as these methods typically require GPU-accelerated optimization for subject-specific inference. Nevertheless, multi-orientation methods continue to play a crucial role in the development of single-orientation methods by serving as reference standards for training, validation, and benchmarking.

In addition to COSMOS, Susceptibility Tensor Imaging (STI) [26] has been adopted as a reference standard in several single-orientation QSM studies [21], [33], [46]. STI extends QSM by modeling susceptibility as a tensor quantity and can better characterize the anisotropic susceptibility behavior in white matter [47]. However, the STI has limited clinical applicability as it generally requires six to twelve orientations, and the commonly used $\chi_{33}$ component may not provide a reliable reference susceptibility map owing to unaccounted phase contributions from off-diagonal tensor terms ($\chi_{13}$ and $\chi_{23}$), whose amplitudes can reach up to approximately 70% of $\chi_{33}$ [21]. Nevertheless, we evaluated the reliability of the STI using simulated datasets, where $\chi_{33}$ reconstructed using eight orientations appeared visually noisy across all datasets and exhibited an NRMSE of approximately 150% for the SIM1 SNR1 case, versus 37% and 26% for COSMOS and OMNIS, respectively, relative to the ground truth. The improved agreement of OMNIS with the ground truth suggests its potential as an *in vivo* reference map for single-orientation QSM evaluations.

Despite the promising performance of OMNIS, several limitations remain. Similar to COSMOS and NDI, OMNIS does not fully account for anisotropic tissue effects, which may lead to magnitude errors. Addressing this issue within the OMNIS framework remains an important area for future studies. Multi-orientation data were generated in the most practical manner using available resources. The simulations used an isotropic scalar susceptibility phantom, whose convolution with the dipole kernel captures only macroscopic field variations and does not account for structural susceptibility anisotropy within a voxel or mesoscopic field effects [48], [49]. A more comprehensive simulation framework could also account for orientation-dependent coil sensitivity variations, $R_2^*$ inhomogeneity, chemical shift effects, or motion artifacts; however, methods to reliably model these effects in this setting remain to be established.

## VI. Conclusion

This study proposed OMNIS, a new iterative method for multi-orientation QSM reconstruction, and presented the first systematic validation using a simulated multi-orientation dataset. A key contribution of this study was demonstrating that comparable or superior susceptibility maps can be obtained with fewer orientations than conventional approaches, thereby addressing a major barrier to the clinical adoption of multi-orientation QSM by reducing the scan time and the need for repeated patient repositioning. OMNIS integrates AVEK-style updates with a nonlinear data fidelity formulation, demonstrating an approximately 80% reduction in total gradient evaluations and 50% reduction in reconstruction time compared to iterative methods. Reliable estimation of disease-related biomarkers and successful translation to *in vivo* data further substantiate their clinical utility in real-world neuroimaging workflows. Overall, OMNIS provides a robust, accurate, and computationally efficient framework for susceptibility estimation with enhanced clinical viability and the potential to serve as a reliable *in vivo* reference standard. Future studies will focus on systematic validation across diverse clinical pathologies and evaluation of extracranial applications to further establish their readiness for clinical use.

## Data and Code Availability

The single-orientation RC2 simulated dataset and associated code are available at [50]. The extended multi-orientation dataset generated in this study will be shared upon request. A sample dataset, together with the OMNIS algorithm and complete evaluation code, is publicly available at `https://anonymous.4open.science/r/OMNIS_QSM-8FFF/`

## References

[1] Y. Wang and T. Liu, "Quantitative susceptibility mapping (QSM): Decoding MRI data for a tissue magnetic biomarker," *Magn. Reson. Med.*, vol. 73, no. 1, pp. 82–101, Jan. 2015.

[2] C. Langkammer *et al.*, "Quantitative susceptibility mapping (qsm) as a means to measure brain iron? a post mortem validation study," *NeuroImage*, vol. 62, no. 3, pp. 1593–1599, 2012.

[3] C. Wisnieff *et al.*, "Quantitative susceptibility mapping (qsm) of white matter multiple sclerosis lesions: Interpreting positive susceptibility and the presence of iron," *Magnetic Resonance in Medicine*, vol. 74, no. 2, pp. 564–570, 2015.

[4] B. Xu *et al.*, "Flow compensated quantitative susceptibility mapping for venous oxygenation imaging," *Magnetic Resonance in Medicine*, vol. 72, no. 2, pp. 438–445, 2014.

[5] T. Harada *et al.*, "Quantitative susceptibility mapping: Basic methods and clinical applications," *Radiographics*, vol. 42, no. 4, pp. 1161–1176, Jul. 2022.

[6] D. Su *et al.*, "Projections for prevalence of parkinson's disease and its driving factors in 195 countries and territories to 2050: modelling study of global burden of disease study 2021," *BMJ*, vol. 388, 2025.

[7] L. Xu *et al.*, "Global incidence trends and projections of alzheimer disease and other dementias: an age-period-cohort analysis 2021," *J. Glob. Health*, vol. 15, p. 04156, May 2025.

[8] E. M. Haacke *et al.*, "Quantitative susceptibility mapping: current status and future directions," *Magnetic Resonance Imaging*, vol. 33, no. 1, pp. 1–25, 2015.

[9] A. Deistung *et al.*, "Overview of quantitative susceptibility mapping," *NMR Biomed.*, vol. 30, no. 4, p. e3569, Apr. 2017.

[10] T. Liu *et al.*, "Calculation of susceptibility through multiple orientation sampling (cosmos): A method for conditioning the inverse problem from measured magnetic field map to susceptibility source image in mri," *Magnetic Resonance in Medicine*, vol. 61, pp. 196–204, 2008.

[11] D. G. Gkotsoulias *et al.*, "Chaos and cosmos—considerations on qsm methods with multiple and single orientations and effects from local anisotropy," *Magnetic Resonance Imaging*, vol. 110, pp. 104–111, 2024.

[12] T. Liu *et al.*, "Nonlinear formulation of the magnetic field to source relationship for robust quantitative susceptibility mapping," *Magn. Reson. Med.*, vol. 69, no. 2, pp. 467–476, Feb. 2013.

[13] D. Polak *et al.*, "Nonlinear dipole inversion (NDI) enables robust quantitative susceptibility mapping (QSM)," *NMR Biomed.*, vol. 33, no. 12, p. e4271, Dec. 2020.

[14] H. Li and M. Haltmeier, "The averaged kaczmarz iteration for solving inverse problems," *SIAM Journal on Imaging Sciences*, vol. 11, no. 1, pp. 618–642, 2018.

[15] J. P. Marques *et al.*, "Qsm reconstruction challenge 2.0: A realistic in silico head phantom for mri data simulation and evaluation of susceptibility mapping procedures," *Magnetic Resonance in Medicine*, vol. 86, pp. 526 – 542, 2021.

[16] S. Wang *et al.*, "Noise effects in various quantitative susceptibility mapping methods," *IEEE Transactions on Biomedical Engineering*, vol. 60, no. 12, pp. 3441–3448, 2013.

[17] QSM Challenge 2.0 Organization Committee *et al.*, "QSM reconstruction challenge 2.0: Design and report of results," *Magn. Reson. Med.*, vol. 86, no. 3, pp. 1241–1255, Sep. 2021.

[18] K.-S. Chan and J. P. Marques, "Sepia—susceptibility mapping pipeline tool for phase images," *NeuroImage*, vol. 227, p. 117611, 2021.

[19] A. Karsa and K. Shmueli, "Segue: A speedy region-growing algorithm for unwrapping estimated phase," *IEEE Transactions on Medical Imaging*, vol. 38, no. 6, pp. 1347–1357, 2019.

[20] S. D. Robinson *et al.*, "An illustrated comparison of processing methods for MR phase imaging and QSM: combining array coil signals and phase unwrapping," *NMR Biomed.*, vol. 30, no. 4, p. e3601, Apr. 2017.

[21] C. Langkammer *et al.*, "Quantitative susceptibility mapping: Report from the 2016 reconstruction challenge," *Magn. Reson. Med.*, vol. 79, no. 3, pp. 1661–1673, Mar. 2018.

[22] B. Bilgic *et al.*, "Rapid multi-orientation quantitative susceptibility mapping," *NeuroImage*, vol. 125, pp. 1131–1141, 2016.

[23] D. Zhou *et al.*, "Background field removal by solving the laplacian boundary value problem," *NMR Biomed.*, vol. 27, no. 3, pp. 312–319, Mar. 2014.

[24] C. Denk *et al.*, "The influence of white matter fibre orientation on mr signal phase and decay," *NMR in Biomedicine*, vol. 24, no. 3, pp. 246–252, 2011.

[25] J. Lee *et al.*, "Sensitivity of mri resonance frequency to the orientation of brain tissue microstructure," *Proceedings of the National Academy of Sciences*, vol. 107, no. 11, pp. 5130–5135, 2010.

[26] C. Liu, "Susceptibility tensor imaging," *Magn. Reson. Med.*, vol. 63, no. 6, pp. 1471–1477, Jun. 2010.

[27] G. Du *et al.*, "Quantitative susceptibility mapping of the midbrain in parkinson's disease," *Mov. Disord.*, vol. 31, no. 3, pp. 317–324, Mar. 2016.

[28] W. Huang *et al.*, "Motoric impairment versus iron deposition gradient in the subthalamic nucleus in parkinson's disease," *J. Neurosurg.*, vol. 135, no. 1, pp. 284–290, Jul. 2021.

[29] L. Doniza *et al.*, "Noise propagation and mp-pca image denoising for high-resolution quantitative $r_2^*$, $t_2^*$, and magnetic susceptibility mapping (qsm)," *IEEE Transactions on Biomedical Engineering*, vol. 72, no. 11, pp. 3277–3287, 2025.

[30] H. Wei *et al.*, "Streaking artifact reduction for quantitative susceptibility mapping of sources with large dynamic range," *NMR Biomed.*, vol. 28, no. 10, pp. 1294–1303, Oct. 2015.

[31] F. Schweser *et al.*, "Quantitative susceptibility mapping for investigating subtle susceptibility variations in the human brain," *NeuroImage*, vol. 62, no. 3, pp. 2083–2100, 2012.

[32] J. Yoon *et al.*, "Quantitative susceptibility mapping using deep neural network: Qsmnet," *NeuroImage*, vol. 179, pp. 199–206, 2018.

[33] R. Feng *et al.*, "Modl-qsm: Model-based deep learning for quantitative susceptibility mapping," *NeuroImage*, vol. 240, p. 118376, 2021.

[34] K.-W. Lai *et al.*, "Learned proximal networks for quantitative susceptibility mapping," *Med. Image Comput. Comput. Assist. Interv.*, vol. 12262, pp. 125–135, Oct. 2020.

[35] H. Wei *et al.*, "Learning-based single-step quantitative susceptibility mapping reconstruction without brain extraction," *NeuroImage*, vol. 202, p. 116064, 2019.

[36] Y. Gao *et al.*, "Instant tissue field and magnetic susceptibility mapping from mri raw phase using laplacian enhanced deep neural networks," *NeuroImage*, vol. 259, p. 119410, 2022.

[37] "Plug-and-play latent feature editing for orientation-adaptive quantitative susceptibility mapping neural networks," *Medical Image Analysis*, 2024.

[38] G. Oh *et al.*, "Unsupervised resolution-agnostic quantitative susceptibility mapping using adaptive instance normalization," *Medical Image Analysis*, vol. 79, p. 102477, 2022.

[39] Z. Xiong *et al.*, "Affine transformation edited and refined deep neural network for quantitative susceptibility mapping," *NeuroImage*, vol. 267, p. 119842, 2023.

[40] M. Zhang *et al.*, "Diffusion-qsm: Diffusion model with time-travel and resampling refinement for quantitative susceptibility mapping," *IEEE Transactions on Biomedical Engineering*, vol. 73, no. 4, pp. 1401–1413, 2026.

[41] Z. Xiong *et al.*, "Advancing quantitative susceptibility mapping with 2.5d diffusion models for rapid intracranial hemorrhage quantification," *Magnetic Resonance in Medicine*, vol. 96, no. 2, pp. 596–610, 2026.

[42] H. Qin *et al.*, "Flow-qsm: bridging learned priors and physical models for quantitative susceptibility mapping," *Physics in Medicine Biology*, vol. 71, no. 7, p. 075002, mar 2026.

[43] J. He *et al.*, "msqsm: Morphology-based self-supervised deep learning for quantitative susceptibility mapping," *NeuroImage*, vol. 275, p. 120181, 2023.

[44] M. Zhang *et al.*, "A subject-specific unsupervised deep learning method for quantitative susceptibility mapping using implicit neural representation," *Medical Image Analysis*, vol. 95, p. 103173, 2024.

[45] Z. Xiong *et al.*, "Quantitative susceptibility mapping through model-based deep image prior (modip)," *NeuroImage*, vol. 291, p. 120583, 2024.

[46] Y. Sun *et al.*, "Nonlinear inversion model-driven deep learning method for magnetic resonance imaging (mri) quantitative susceptibility mapping imaging," *Quantitative Imaging in Medicine and Surgery*, vol. 16, no. 2, 2026.

[47] W. Li *et al.*, "Susceptibility tensor imaging (STI) of the brain," *NMR Biomed.*, vol. 30, no. 4, p. e3540, Apr. 2017.

[48] S. Wharton and R. Bowtell, "Effects of white matter microstructure on phase and susceptibility maps," *Magnetic Resonance in Medicine*, vol. 73, no. 3, pp. 1258–1269, 2015.

[49] A. D. Sandgaard *et al.*, "The larmor frequency shift of a white matter magnetic microstructure model with multiple sources," *NMR in Biomedicine*, vol. 37, no. 8, p. e5150, 2024.

[50] J. Marques, "Quantitative Susceptibility Mapping (QSM) Challenge 2.0," 2021. [Online]. Available: https://doi.org/10.34973/m20r-jt17